Supplementary Information for

"Acoustic Spin Skyrmion Molecule Lattices Enabling Stable Transport and Flexible Manipulation"

LEI LIU[1], XIUJUAN ZHANG[1,*], MING-HUI LU[1,2,3,*], AND YAN-FENG CHEN[1,3,*]

[1]*National Laboratory of Solid State Microstructures and Department of Materials Science and Engineering, Nanjing University, Nanjing 210093, China*

[2]*Jiangsu Key Laboratory of Artificial Functional Materials, Nanjing 210093, China*

[3]*Collaborative Innovation Center of Advanced Microstructures, Nanjing University, Nanjing 210093, China*

**Email: xiujuanzhang@nju.edu.cn, luminghui@nju.edu.cn, yfchen@nju.edu.cn*

CONTENTS

1. Tight bonding model of p-orbitals graphene

The coupling between $|p_x\rangle$ and $|p_y\rangle$ orbitals in the graphene lattice can be described by the following tight-binding Hamiltonian

$$H = \sum_{m,n} t_L(\hat{\boldsymbol{\alpha}}^{\dagger}{}_{m,n} \cdot \mathbf{e}_{L1})\,(\mathbf{e}_{L1} \cdot \hat{\boldsymbol{\beta}}^{\dagger}{}_{m,n}) + t_L(\hat{\boldsymbol{\alpha}}^{\dagger}{}_{m,n} \cdot \mathbf{e}_{L2})\,(\mathbf{e}_{L2} \cdot \hat{\boldsymbol{\beta}}^{\dagger}{}_{m+1,n}) + t_L(\hat{\boldsymbol{\alpha}}^{\dagger}{}_{m,n} \cdot \mathbf{e}_{L3})\,(\mathbf{e}_{L3} \cdot \hat{\boldsymbol{\beta}}^{\dagger}{}_{m,n+1}) + t_T(\hat{\boldsymbol{\alpha}}^{\dagger}{}_{m,n} \cdot \mathbf{e}_{T1})\,(\mathbf{e}_{T1} \cdot \hat{\boldsymbol{\beta}}^{\dagger}{}_{m,n}) + t_T(\hat{\boldsymbol{\alpha}}^{\dagger}{}_{m,n} \cdot \mathbf{e}_{T2})\,(\mathbf{e}_{T2} \cdot \hat{\boldsymbol{\beta}}^{\dagger}{}_{m+1,n}) + t_T(\hat{\boldsymbol{\alpha}}^{\dagger}{}_{m,n} \cdot \mathbf{e}_{T3})\,(\mathbf{e}_{T3} \cdot \hat{\boldsymbol{\beta}}^{\dagger}{}_{m,n+1}) + h.c.\,, \tag{S1.1}$$

where $\mathbf{e}_{L1,L2,L3}$ are unit vectors oriented parallel to each site's nearest-neighbor links (see Fig. 2a), while $\mathbf{e}_{T1,T2,T3}$ are unit vectors oriented perpendicular to those links. $\hat{\boldsymbol{\alpha}}^{\dagger}{}_{m,n} = \left[\hat{\alpha}^{\dagger}{}_{m,n,p_x}, \hat{\alpha}^{\dagger}{}_{m,n,p_y}\right]$ and $\hat{\boldsymbol{\beta}}^{\dagger}{}_{m,n} = \left[\hat{\beta}^{\dagger}{}_{m,n,p_x}, \hat{\beta}^{\dagger}{}_{m,n,p_y}\right]$ are the creation operators for the $|p_x\rangle$ or $|p_y\rangle$ orbitals at sites α, β of the (m,n)-th unit cell. The (p_x, p_y) doublet obeys the E irrep of C_{3v} site symmetry in the graphene lattice[1]. Considering the hopping of orbitals oriented perpendicular to the links is negligible ($t_T = 0$), the Hamiltonian in Eq. (S1.1) can be expressed in momentum space in the form of Eq. (1) of the main text. Solving the eigenequation $H(\mathbf{k})|\psi(\mathbf{k})\rangle = E(\mathbf{k})|\psi(\mathbf{k})\rangle$ yields the dispersion relations of four bands

$$E_{1,4} = \mp\frac{3t_L}{2}, \qquad E_{2,3} = \mp\frac{t_L}{2}\sqrt{3 + 2\sum_i \cos\mathbf{k}\cdot\mathbf{b}_i}\,, \tag{S1.2}$$

where $\mathbf{b}_i = -\frac{1}{2}\boldsymbol{\epsilon}_{ijk}(\mathbf{e}_j - \mathbf{e}_k)$. These four bands, labeled 1 to 4 from bottom to top, are shown in Fig. 2b. The band structure features two flat bands $E_{1,4}$ over the entire 2D Brillouin zone. Their corresponding eigenvectors can be found analytically as

$$|\psi\rangle_{1,4} = \Omega\left(\frac{1}{\sqrt{3}}(f_{21}^* - f_{13}^*), -f_{32}^*, \pm\frac{1}{\sqrt{3}}(f_{21} - f_{13}), \mp f_{32}\right)^T, \tag{S1.3}$$

where $\Omega = \left[\frac{8}{3}(3 - \sum_i \cos\mathbf{k}\cdot\mathbf{b}_i)\right]^{-\frac{1}{2}}$ and $f_{mn} = e^{i\mathbf{k}\cdot\mathbf{e}_m} - e^{i\mathbf{k}\cdot\mathbf{e}_n}$. Specially, the $E_{2,3}$ bands exhibit Dirac cone structures. To simplify the analysis, we construct a set of basis vectors, orthogonal to $|\psi\rangle_{1,4}$, which spans the subspace corresponding to the Dirac bands $E_{2,3}$

$$|\psi_\alpha\rangle = \sqrt{2}\Omega\left(f_{32}^*, \frac{1}{\sqrt{3}}(f_{21}^* - f_{13}^*), 0, 0\right)^T,$$

$$|\psi_\beta\rangle = \sqrt{2}\Omega\left(0, 0, f_{32}, \frac{1}{\sqrt{3}}(f_{21} - f_{13})\right)^T. \tag{S1.4}$$

Within this subspace, the Hamiltonian takes the form

$$H_{2,3}(\mathbf{k}) = -\frac{t_L}{2}\begin{bmatrix} 0 & \sum_n e^{i\mathbf{k}\cdot\mathbf{e}_n} \\ \sum_n e^{-i\mathbf{k}\cdot\mathbf{e}_n} & 0 \end{bmatrix}, \tag{S1.5}$$

which is identical to the graphene Hamiltonian. Two Dirac cones appear at the valleys $K = \left(\frac{4\pi}{3a}, 0\right)$

and $K' = \left(-\frac{4\pi}{3a}, 0\right)$, as well as at other equivalent energy valleys. The eigenvectors of the $E_{2,3}$ bands read

$$|\psi\rangle_{2,3} = \frac{1}{\sqrt{2}}\left(|\psi_\alpha\rangle \pm e^{i\theta_k}|\psi_\beta\rangle\right)^T, \qquad \text{with } \theta_k = \arg\left(\sum_n e^{i\mathbf{k}\cdot\mathbf{e}_n}\right), \tag{S1.6}$$

For the sake of simplicity, these eigenstates can be rewritten as

$$|\psi\rangle_{2,3} = \frac{1}{\sqrt{2}}\begin{pmatrix} |\psi_\alpha\rangle \\ \pm e^{i\theta_k}|\psi_\beta\rangle \end{pmatrix} \propto \begin{pmatrix} |p_x\rangle + \mathcal{Q}|p_y\rangle \\ \pm e^{i\theta_k}(|p_x\rangle + \mathcal{Q}^*|p_y\rangle) \end{pmatrix}, \qquad \text{with } \mathcal{Q}(\mathbf{k}) = \frac{(f_{21}^* - f_{13}^*)}{\sqrt{3}f_{32}^*}, \tag{S1.7}$$

Clearly, these eigenstates at each site are superpositions of the $|p_x\rangle$ and $|p_y\rangle$ orbitals. Analogous to converting Hermite–Gaussian modes into Laguerre–Gaussian modes, these superposed eigenstates carry nontrivial chirality or angular momentum. We define the chirality of the eigenstates at sites α and β as

$$\begin{aligned} \mathcal{C}_\alpha &\propto \mathrm{Im}\left[\sqrt{3}f_{32}(f_{21}^* - f_{13}^*) - \sqrt{3}f_{32}^*(f_{21} - f_{13})\right], \\ \mathcal{C}_\beta &\propto \mathrm{Im}\left[\sqrt{3}f_{32}^*(f_{21} - f_{13}) - \sqrt{3}f_{32}(f_{21}^* - f_{13}^*)\right], \end{aligned} \tag{S1.8}$$

as shown in Fig. S1a. Three key observations follow:

(1) The chiralities at sites α and β are opposite. $\mathcal{C}_\alpha$ and $\mathcal{C}_\beta$ have opposite signs, and this is radically protected by the inversion symmetry $\mathcal{P}$ (or sublattice symmetry), as

$$|\psi_\beta\rangle = \mathcal{P}|\psi_\alpha\rangle = \mathcal{P}|p_x\rangle + \mathcal{Q}(-\mathbf{k})\mathcal{P}|p_y\rangle = |p_x\rangle + \mathcal{Q}^*|p_y\rangle. \tag{S1.9}$$

(2) Additionally, the chiralities of eigenstates at these two valleys invert under time-reversal symmetry, as given by $|\psi_K\rangle = \mathcal{T}|\psi_{K'}\rangle$.

(3) Perfect vortices appear at the valleys. Due to the C_{3v} symmetry of the graphene lattice, these eigenstates at the valley, consisting of $|p_x\rangle$ and $|p_y\rangle$ orbitals, must adhere to this symmetry and naturally form vortices. The chirality of eigenstates depends on the values of $\mathcal{Q}$, which is related with the Bloch momentum, as shown in Fig. S1b. In particular, $\mathcal{Q} = \mp i$ at the K and K' valley, transforming the eigenstates into

$$\begin{aligned} |\psi_K\rangle &\propto \begin{pmatrix} |p_x\rangle - i|p_y\rangle \\ \pm(|p_x\rangle + i|p_y\rangle) \end{pmatrix} = \begin{pmatrix} |\Psi_-\rangle \\ \pm|\Psi_+\rangle \end{pmatrix}, \\ |\psi_{K'}\rangle &\propto \begin{pmatrix} |p_x\rangle + i|p_y\rangle \\ \pm(|p_x\rangle - i|p_y\rangle) \end{pmatrix} = \begin{pmatrix} |\Psi_+\rangle \\ \pm|\Psi_-\rangle \end{pmatrix}, \end{aligned} \tag{S1.10}$$

where $|\Psi_\pm\rangle = |p_x\rangle \pm i|p_y\rangle$ represent vortices with topological charges of ± 1, respectively. These results match the chirality spectrum shown in Fig. S1a. The phase of $\mathcal{Q}$ plays a pivotal role in determining the chirality of the eigenstates. In the main text, the phase difference $\mathcal{D}$ between $|p_x\rangle$ and $|p_y\rangle$ components is related to the phase of $\mathcal{Q}$ for the Dirac bands by

$$\mathcal{D} = \arg\left(\frac{\phi_{i,p_y}}{\phi_{i,p_x}}\right) = \begin{cases} \arg(\mathcal{Q}), & i = \alpha \\ \arg(\mathcal{Q}^*), & i = \beta \end{cases}. \tag{S1.11}$$

Moreover, the parameter θ_k determines the parity of the eigenstates between the two sites, as shown in Fig. S1c. On the valley lines (indicated by the white dashed line), θ_k is either 0 or π, yielding eigenstates with even parity ($|\psi_\alpha\rangle + |\psi_\beta\rangle$) or odd parity ($|\psi_\alpha\rangle - |\psi_\beta\rangle$).

In summary, the interaction between anisotropic degenerate p-orbitals and the graphene lattice gives rise to eigenstates with chirality that evolves with Bloch momentum. Remarkably, the

eigenstates at valleys are restricted by the lattice symmetry, thereby exhibiting valley-locked vortex-antivortex pairs.

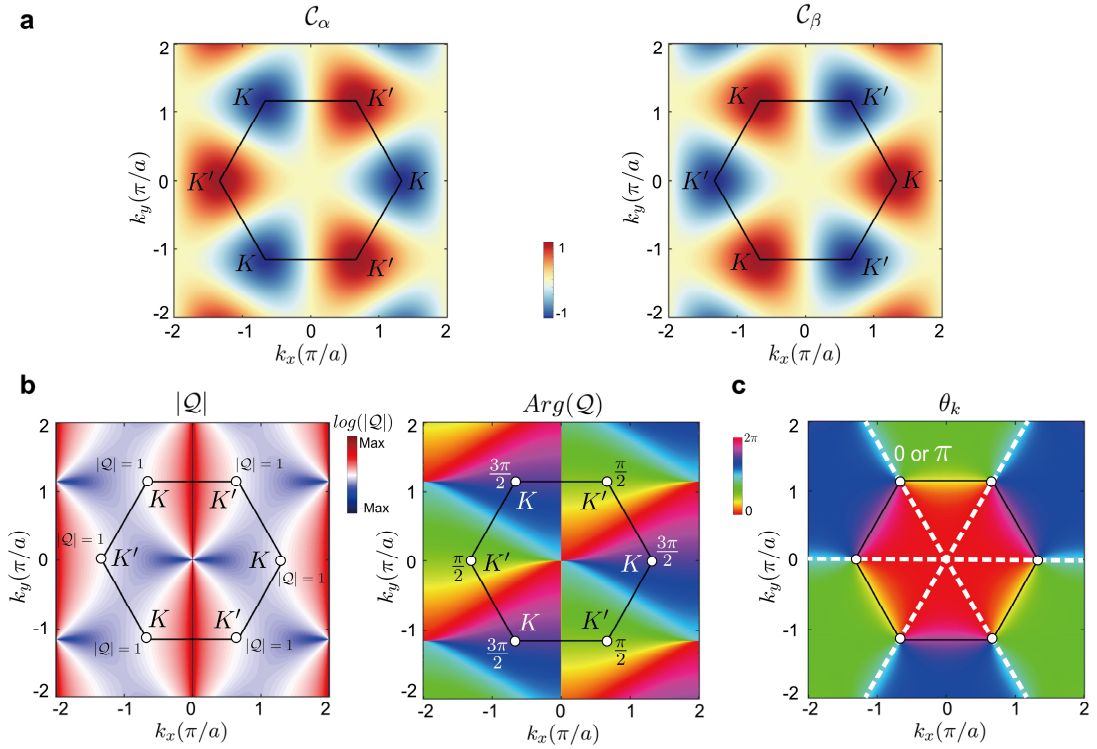

Fig. S1. **a**, Chiralities of eigenstates at sites α, β. **b**, Left panel: Magnitude of $\mathcal{Q}$, which equals 1 at the valleys; Right panel: Phase of $\mathcal{Q}$, which is $\frac{\pi}{2}$ at the K valley while $\frac{3\pi}{2}$ at the K' valley. **c**, Distribution of θ_k. It is 0 or π along the valley lines, indicated by the white dashed lines.

2. Intrinsic spin skyrmions in evanescent vortices

Vortices intrinsically carry out-of-plane spin, whereas evanescent waves intrinsically carry in-plane spin. Consequently, evanescent vortices feature a full spin vector field. Due to the unique configuration of the vortex field, the corresponding spin vector field encompasses all possible spin orientations, forming a spin skyrmion. To validate this, we consider a Gaussian acoustic vortex described by

$$P(x,y) = p_0(x + i \cdot sign(l) \cdot y)^{|l|} \cdot exp\left(-\frac{x^2+y^2}{\varpi^2}\right) \cdot exp(-\kappa z), \tag{S2.1}$$

where ϖ is the radius of the Gaussian field, p_0 is the given amplitude (initial pressure), l is the topological charge of the vortex, and κ is the spatial decay factor. Taking $\varpi = \lambda$ and $\kappa = 63\lambda$, the intensity and phases of vortices with topological charges $l = \pm 1$ are shown in Figs. S2a and c. From the incompressible linear Euler equation,

$$\rho \frac{\partial \mathbf{v}}{\partial t} = -\nabla P, \tag{S2.2}$$

where ρ represents the mass density and $\mathbf{v}$ denotes the velocity field, and assuming time-harmonic acoustic waves, we can rewrite Eq. (S2.2) as

$$\mathbf{v} = \frac{i}{\rho\omega}\nabla P. \tag{S2.3}$$

It follows that the acoustic velocity field of the vortex can be derived as

$$\mathbf{v}[v_x, v_y, v_z] = C\left[\frac{-i2x^2 + 2xy \cdot sign(l) + i|l|\varpi^2}{\varpi^2(-y \cdot sign(l) + ix)}, \frac{2 \cdot sign(l) \cdot y^2 - i2xy - |l|\varpi^2}{\varpi^2(-y \cdot sign(l) + ix)}, -\kappa\right], \tag{S2.4}$$

where

$$C = \frac{ip_0}{2\rho\omega}(x + i \cdot sign(l) \cdot y)^{|l|} \cdot exp\left(-\frac{x^2+y^2}{\varpi^2}\right) \cdot exp(-\kappa z). \tag{S2.5}$$

Using this velocity field, the acoustic spin density can be calculated via

$$\mathbf{s} = \frac{\rho}{2\omega}\mathrm{Im}(\mathbf{v}^* \times \mathbf{v}). \tag{S2.6}$$

We focus on the direction of the spin vector and normalize the spin field as $\hat{\mathbf{s}} = \mathbf{s}/|\mathbf{s}|$. The spin vector field $\hat{\mathbf{s}}$ for the vortices with topological charge $l = \pm 1$ are shown in Figs. S2b and S2d. Notably, the spin direction flips along the radial direction, exhibiting Néel-type skyrmions. Such topological structure is characterized by the skyrmion number defined as

$$n_{sk} = \frac{1}{4\pi}\iint d_{sk}(x,y)\,dx\,dy = \frac{1}{4\pi}\iint \hat{\mathbf{s}} \cdot \left(\frac{\partial \hat{\mathbf{s}}}{\partial x} \times \frac{\partial \hat{\mathbf{s}}}{\partial x}\right) dx\,dy, \tag{S2.7}$$

where d_{sk} is the skyrmion density. These densities for vortices with $l = \pm 1$ are shown in the insets of Figs. S2b and S2d. By integrating the skyrmion density over the xy-plane, we find that that evanescent vortices with topological charges $l = \pm 1$ correspond to skyrmions with $n_{sk} = \pm 1$,

respectively. Furthermore, since $\hat{s}_x{}^2 + \hat{s}_y{}^2 + \hat{s}_z{}^2 = 1$, the spin vectors in the 3D parameter space $\mathbb{R}^3$ can map onto the 2D unit sphere $\mathbb{S}^2$. Thus, the skyrmion number can be phenomenologically understood as the number of times the vectors wrap around a unit sphere. In an example of a skyrmion with $n_{sk} = 1$, the spin vectors from the skyrmion center to its boundary are mapped onto a sphere from the north pole to the south pole (Fig. S2b), whereas for $n_{sk} = -1$, they extend from the south pole to the north pole (Fig. S2d).

The above analysis confirms that evanescent acoustic pressure vortices are intrinsic velocity spin skyrmions. This fundamentally arises from the gradient relationship between the velocity vector field and the pressure scalar field, a principle that can be generalized to other physical systems possessing analogous gradient relationships. For instance, Eq. (S2.2) also applies to low-amplitude incompressible liquids, while in uniform media, transverse magnetic (TM) waves obey a similar gradient relationship between the magnetic vector field $\mathbf{H}$ and the electric scalar field E_z, expressed as $\mathbf{H} = -\frac{i}{\mu\omega}\nabla E_z$ (where μ is the permeability).

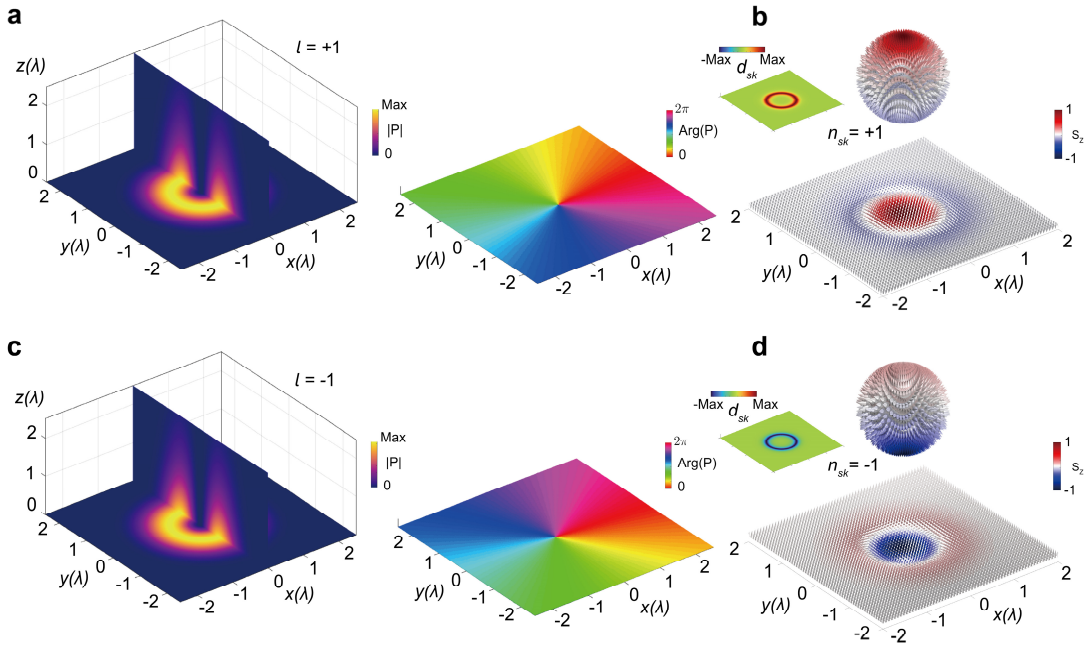

Fig. S2. **a** and **c**, Intensity and phases of vortices with topological charges $l = \pm 1$. **b** and **d**, Spin vector fields of the corresponding vortices in (a) and (c), plotted on the xy-plane at $z = 0$. The insets depict the spin vectors stereographically projected onto a unit sphere, alongside the corresponding the distributions of skyrmion density.

3. Valley-locked molecule lattices and robust propagation

In real space, the K' valley-locked vortex molecule lattice can be considered as vortex molecules modulated by a valley-locked triangular lattice. This can be expressed as the convolution between the vortex molecules $\Psi_{\text{molecule}}(\mathbf{r})$ and a valley-locked triangular lattice Dirac comb δ_{valley}, as

$$\Psi(\mathbf{r}) = \Psi_{\text{molecule}}(\mathbf{r}) * \delta_{valley}(\mathbf{r}), \tag{S3.1}$$

where $\mathbf{r} = (x, y)$ is the position vector. The valley-locked triangular lattice Dirac comb consists of a triangular lattice Dirac comb and a valley-locked plane wave background field $\Psi_{\text{plane}}(\mathbf{r})$, given by

$$\delta_{valley}(\mathbf{r}) = \sum_{n,m} \delta(\mathbf{r} - \mathbf{g}) \cdot \Psi_{\text{plane}}(\mathbf{r}), \tag{S3.2}$$

where $\mathbf{g} = n\boldsymbol{a}_1 + m\boldsymbol{a}_2$ is the lattice vector with $\boldsymbol{a_1} = \frac{a}{2}(1, \sqrt{3})$ and $\boldsymbol{a_2} = \frac{a}{2}(-1, \sqrt{3})$, and a is the lattice constant. The valley-locked and propagating forward plane wave background field $\Psi_{\text{plane}}(\mathbf{r})$ is expressed as

$$\Psi_{\text{plane}}(\mathbf{r}) = \begin{cases} e^{-i\boldsymbol{K'}_1\mathbf{r}} + e^{-i\boldsymbol{K'}_2\mathbf{r}}, \boldsymbol{K'}_{1,2} = \left(\frac{2\pi}{3a}, \pm\frac{2\pi}{3\sqrt{3}a}\right) \text{for } K' \text{ valley} \\ e^{-i\boldsymbol{K}\mathbf{r}}, \quad \boldsymbol{K} = (\frac{4\pi}{3a}, 0) \text{ for } K \text{ valley} \end{cases}. \tag{S3.3}$$

The field of vortex molecules Ψ_{molecule} is written as

$$\Psi_{\text{molecule}}(\mathbf{r}) = \begin{cases} \psi_\alpha(\mathbf{r}) + \psi_\beta(\mathbf{r}), & \text{for even molecule} \\ \psi_\alpha(\mathbf{r}) - \psi_\beta(\mathbf{r}), & \text{for odd molecule} \end{cases}, \tag{S3.4}$$

where $\psi_\alpha(\mathbf{r})$ and $\psi_\beta(\mathbf{r})$ are the vortex fields at sites α and β, respectively, expressed as

$$\begin{aligned} \psi_\alpha(\mathbf{r}) &= [(x - x_\alpha) + i \cdot sign(l) \cdot (y - y_\alpha)]^{|l|} \cdot e^{-\frac{|\mathbf{r}-\mathbf{r}_\alpha|}{\varpi^2}}, \\ \psi_\beta(\mathbf{r}) &= \left[(x - x_\beta) + i \cdot sign(l) \cdot (y - y_\beta)\right]^{|l|} \cdot e^{-\frac{|\mathbf{r}-\mathbf{r}_\beta|}{\varpi^2}}, \end{aligned} \tag{S3.5}$$

where l is the topological charge of the vortex. Here, we consider the even vortex molecule at the K' valley, comprising one vortex with a topological charge of $+1$ at site α and another with a topological charge of -1 at site β. Taking the Gaussian field radius $\varpi = 0.2a$, the even vortex molecule is shown in Fig. S3a. The K' valley-locked triangular lattice Dirac comb is shown in Fig. S3b. By convolving these two components, the K' valley-locked vortex molecule lattice is constructed, as shown in Fig. S3c, which agrees with the measured results in Fig. 3d.

Based on convolution theorem, the Fourier decomposition of the vortex molecule lattice can be written as

$$\widetilde{\Psi}(\mathbf{k}) = \mathcal{F}\{\Psi_{\text{molecule}}(\mathbf{r}) * \delta_{valley}(\mathbf{r})\} = \mathcal{F}\{\Psi_{\text{molecule}}(\mathbf{r})\} \cdot \mathcal{F}\{\delta_{valley}(\mathbf{r})\}, \tag{S3.6}$$

where $\mathcal{F}$ denotes the Fourier transform operator. The Fourier transform of the even vortex molecule is expressed as

$$\widetilde{\Psi}_{\text{molecule}}(\mathbf{k}) = \mathcal{F}\{\Psi_{\text{molecule}}(\mathbf{r})\} = e^{-\varpi^2|\mathbf{k}|^2}\left[e^{i\mathbf{k}\mathbf{r}_\alpha}(ik_x - k_y) + e^{i\mathbf{k}\mathbf{r}_\beta}(ik_x + k_y)\right], \tag{S3.7}$$

and the intensity distribution is shown in Fig. S3d. The Fourier transform of the valley-locked triangular lattice Dirac comb is

$$\tilde{\delta}_{valley}(\mathbf{r}) = \mathcal{F}\left[\delta_{valley}(\mathbf{r})\right] = \mathcal{F}\left[\sum_{n,m} \delta(\mathbf{r} - \mathbf{g})\right] * \mathcal{F}\left[\widetilde{\Psi}_{\text{plane}}(\mathbf{r})\right]$$

$$= \sum\nolimits_{n',m'} [\delta(\mathbf{k} - (\mathbf{G} + \boldsymbol{K'_1}) + \delta(\mathbf{k} - (\mathbf{G} + \boldsymbol{K'_2})], \tag{S3.8}$$

where $\mathbf{G} = n'\boldsymbol{b_1} + m'\boldsymbol{b_2}$ is the reciprocal lattice vector with $\boldsymbol{b_1} = \frac{4\pi}{3a}(\sqrt{3}, 1)$ and $\boldsymbol{b_2} = \frac{4\pi}{3a}(-\sqrt{3}, 1)$. The distribution of the Fourier transform of the valley-locked triangular lattice Dirac comb is shown in Fig. S3e, exhibiting a K' valley-locked Dirac comb. Therefore, by taking the dot product between the Fourier transform of the even vortex molecule and the K' valley-locked triangular lattice Dirac comb, we obtain the Fourier transform of the K' valley-locked vortex molecule lattice

$$\begin{aligned}\widetilde{\Psi}(\mathbf{k}) = \sum_{n',m'} & e^{-\varpi^2|\mathbf{G}+\boldsymbol{K'}_1|^2}\{e^{i(\mathbf{G}+\boldsymbol{K'}_1)\boldsymbol{r}_\alpha}[i(G_x + K'_{1x}) - (G_y + K'_{1y})] + e^{i(\mathbf{G}+\boldsymbol{K'}_1)\boldsymbol{r}_\beta}[i(G_x + K'_{1x}) \\ & + (G_y + K'_{1y}]\}\delta(\mathbf{k} - (\mathbf{G} + \boldsymbol{K'}_1) \\ & + \sum_{n',m'} e^{-\varpi^2|\mathbf{G}+\boldsymbol{K'}_2|^2}\{e^{i(\mathbf{G}+\boldsymbol{K'}_2)\boldsymbol{r}_\alpha}[i(G_x + K'_{2x}) - (G_y + K'_{2y})] \\ & + e^{i(\mathbf{G}+\boldsymbol{K'}_2)\boldsymbol{r}_\beta}[i(G_x + K'_{2x}) + (G_y + K'_{2y}]\}\delta(\mathbf{k} - (\mathbf{G} + \boldsymbol{K'}_2),\end{aligned} \tag{S3.9}$$

as shown in Fig. S3f, which is consistent with the Fourier transform results of the measured K' valley-locked even vortex molecule lattice (the right plane of Fig. 3d).

We further embed this molecule lattice in an evanescent field, expressed as

$$\Psi_{\text{evanescent}}(\mathbf{r}, z) = \Psi(\mathbf{r})e^{-\kappa z}, \tag{S3.10}$$

where κ is the spatial decay factor. The gradient vector field of this scalar field is then given by

$$\boldsymbol{\mathcal{V}} = \nabla\Psi_{\text{evanescent}}. \tag{S3.11}$$

Using this vector field, the spin density can be computed as

$$\mathbf{s} = \text{Im}(\boldsymbol{\mathcal{V}}^* \times \boldsymbol{\mathcal{V}}). \tag{S3.12}$$

Considering $\kappa = 5a$, the resulting spin vector field $\hat{\mathbf{s}} = \mathbf{s}/|\mathbf{s}|$ is shown in Fig. S3g. It exhibits an even skyrmion molecule lattice, which agrees with the measured result in Fig. 3c.

We also theoretically construct the K valley-locked odd vortex and skyrmion molecule lattices, as shown in Fig. S4, which are consistent with the measured results in Fig. 4d.

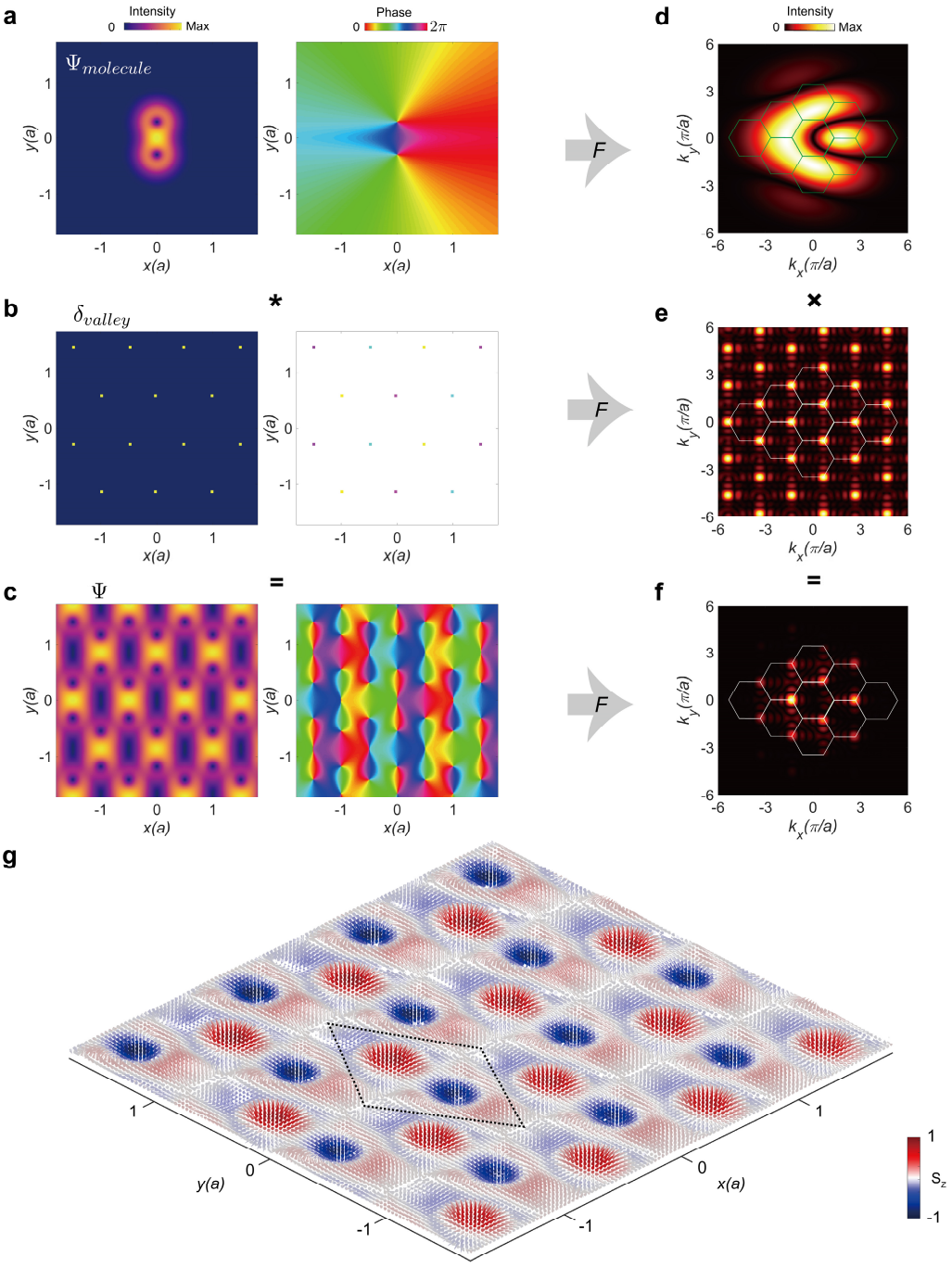

Fig. S3. **a**, Intensity and phase distributions of an even vortex molecule. **b,** Intensity and phase distributions of the K' valley-locked triangular lattice Dirac comb. **c**, Intensity and phase distributions of the K' valley-locked even vortex molecule lattice, generated by convolving (a) and (b). **d, e** and **f**, Intensity distributions of the Fourier transforms of (a), (b), and (c), respectively. In Fourier space, convolution in real space corresponds to multiplication. **g**, Spin vector field derived from the scalar field in (c).

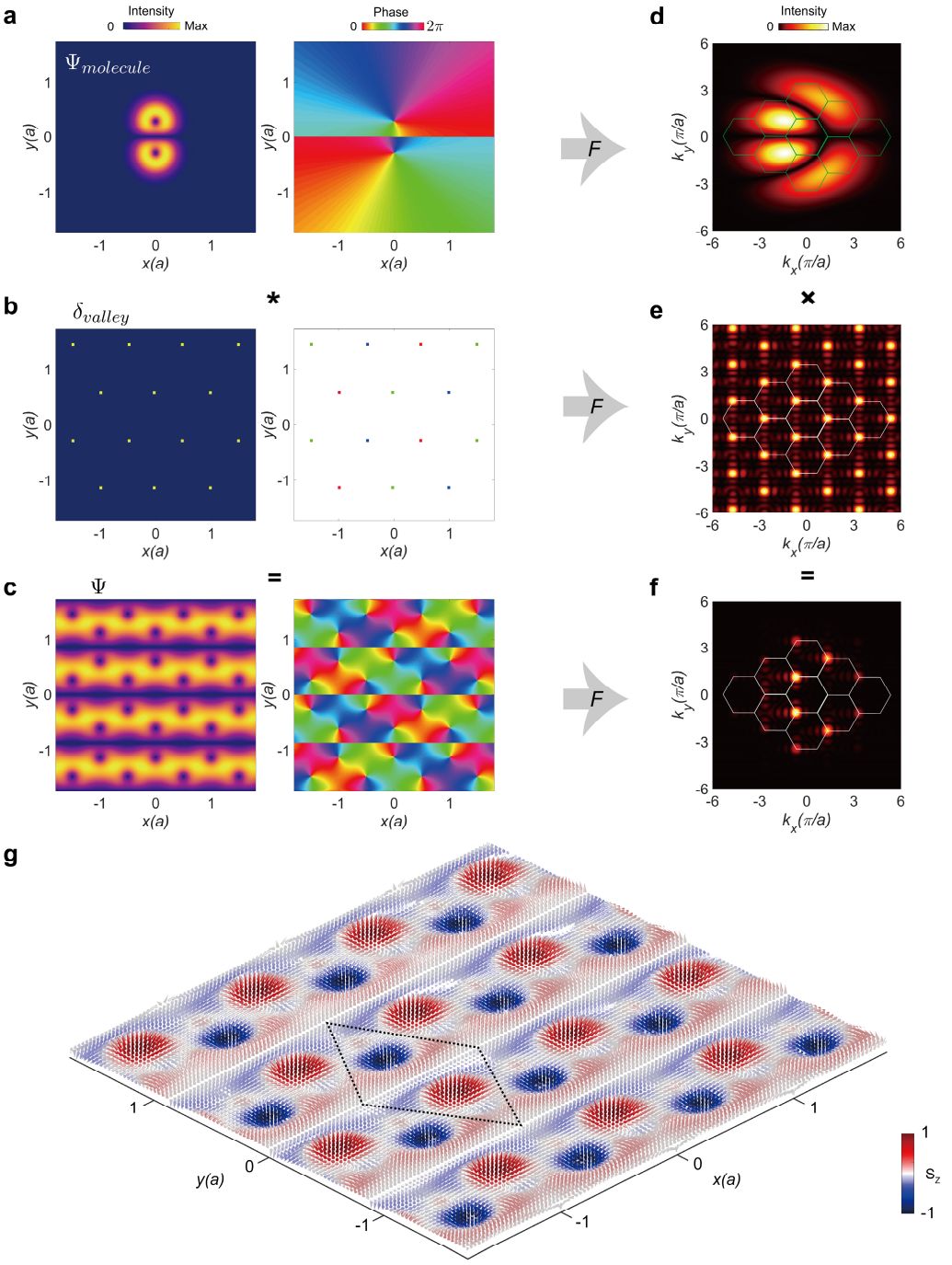

Fig. S4. **a**, Intensity and phase distributions of an odd vortex molecule. **b**, Intensity and phase distributions of the K valley-locked triangular lattice Dirac comb. **c**, Intensity and phase distributions of the K valley-locked odd vortex molecule lattice, generated by convolving (a) and (b). **d**, **e** and **f**, Intensity distributions of the Fourier transforms of (a), (b), and (c), respectively. **g**, Spin vector field derived from the scalar field in (c).

Due to the valley-locked property, the transport of skyrmion molecules exhibits immunity against sharp bends, providing protection comparable to that of valley Hall-type topological transport[2]. To verify this, a structure with 120-degree bends is designed, as shown in Fig. S5a. The acoustic field is excited from the left side of the structure, and the acoustic field distribution at 3.625 kHz remains as an extended vortex molecule lattice (Fig. S5a) and skyrmion molecule lattice (Fig. S5b). Specifically, the spin vector after propagating through the 120-degree bends still exhibits skyrmion

molecules, as shown in the insets of Fig. S5b. This indicates that the sharp bends do not compromise the transmission of the vortex and skyrmion molecules. The observed robustness originates from the equivalence of different K' valleys. Different K' valleys possess identical chiral eigenmodes but with varying wavevector directions. However, eigenmodes with inverse wavevector directions, corresponding to the K valleys, carry inverse chirality and are orthogonal to those at the K' valleys. Consequently, when the sound field encounters bends, it tends to couple to the same chiral eigenmode, resulting in K' valley-locked propagation and immunity against backscattering.

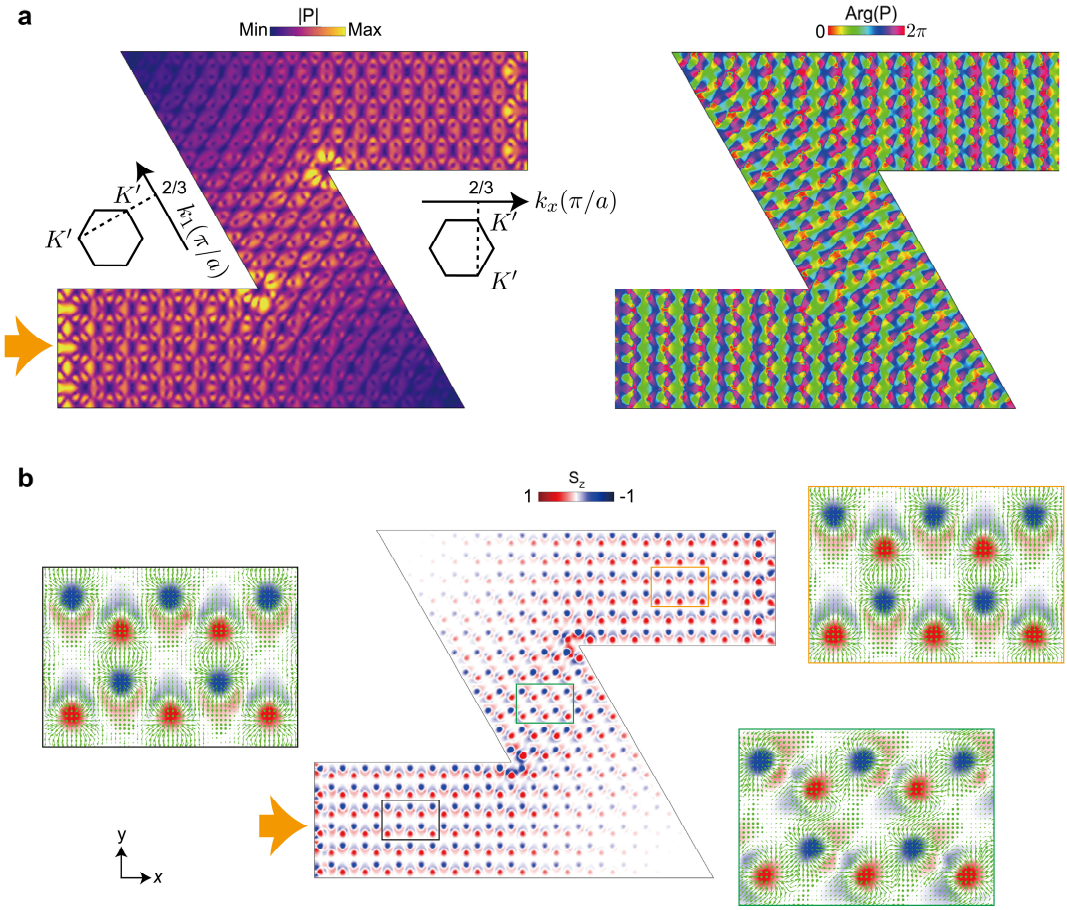

Fig. S5. **a**, Simulated acoustic pressure field and its phase distributions at 3.625 kHz, excited from the left side of the structure (indicated by the yellow arrow). The inset displays the propagating momentum along the x-axis and the 120-degree bend, both locked by the K' valleys. **b**, Spin density s_z distribution. The inset planes show the spin vector fields for the regions highlighted by the boxes. All the xy-planes are located at $z = h_a/2$.

4. Scalability of the molecule lattice

In the main text, the vortex and skyrmion molecule bulk states are induced by the boundary conditions, making them independent of the lattice width and thus scalable. Figure S6a shows a finite graphene ribbon with N unit cells in the y-direction. In the subspace of the Dirac bands $E_{2,3}$, the eigenstates on each site are treated as a single superimposed state of the $|p_x\rangle$ and $|p_y\rangle$ orbitals, as described by Eq. (S1.4), thereby reducing the p-orbitals graphene model to a general graphene model given by Eq. (S1.5). Consequently, under boundary conditions, the Hamiltonian for the graphene ribbon can be written as

$$H_{\mathrm{GR}}(k_x, E_{\mathrm{edge}}) = -\frac{t_L}{2}\begin{bmatrix} \mathcal{U}_1 & \mathcal{C} & 0 & 0 & 0 \\ \mathcal{C}^\dagger & \mathcal{P} & \ddots & 0 & 0 \\ 0 & \mathcal{C}^\dagger & \ddots & \mathcal{C} & 0 \\ 0 & 0 & \ddots & \mathcal{P} & \mathcal{C} \\ 0 & 0 & 0 & \mathcal{C}^\dagger & \mathcal{U}_2 \end{bmatrix}, \tag{S4.1}$$

in the basis $|\psi_{\mathrm{GR}}\rangle = \left(\phi_{\alpha_1}, \phi_{\beta_1}, \cdots, \phi_{\alpha_{\mathrm{N}}}, \phi_{\beta_{\mathrm{N}}}\right)^T$. Here, $\mathcal{U}_{1,2}$, $\mathcal{P}$ and $\mathcal{C}$ represent the boundary, bulk, and link blocks, respectively, and are defined as

$$\mathcal{U}_1 = \begin{bmatrix} E_{\mathrm{edge}} & 2cos\frac{k_x}{2} \\ 2cos\frac{k_x}{2} & 0 \end{bmatrix}, \tag{S4.2}$$

$$\mathcal{U}_2 = \begin{bmatrix} 0 & 2cos\frac{k_x}{2} \\ 2cos\frac{k_x}{2} & E_{\mathrm{edge}} \end{bmatrix}, \tag{S4.3}$$

$$\mathcal{P} = \begin{bmatrix} 0 & 2cos\frac{k_x}{2} \\ 2cos\frac{k_x}{2} & 0 \end{bmatrix}, \tag{S4.4}$$

$$\mathcal{C} = \begin{bmatrix} 0 & 0 \\ 1 & 0 \end{bmatrix}. \tag{S4.5}$$

The boundary potential is controlled by the energy E_{edge} at sites α_1 and β_{N}. When the boundary potentials match the average bulk potential (i.e., the coupling strength between sites), the chiral anomaly bulk states emerge (see Supplementary Information 5 for details). Setting the boundary potential to -1, the band structure for $\mathrm{N} = 12$ is calculated and shown in Fig. S6b. The chiral anomaly bulk state appears in the bandgap, and the bandgap width ΔE depends on the energy window at valleys. The energy at the valley is given by

$$E_i = -t_L \cos\frac{i\pi}{2\mathrm{N}}, i = 1,2,\cdots,2\mathrm{N}. \tag{S4.6}$$

Thus, the energy window is defined as $\Delta E = |E_{\mathrm{N}+1} - E_{\mathrm{N}-1}|$. By Taylor expansion, it can be rewritten as

$$\Delta E = \left|\frac{\pi t_L}{\mathrm{N}}\right|, \tag{S4.7}$$

which is inversely proportional to N. This indicates that as the width increases, the energy window ΔE narrows.

For further verifying this relationship, we simulate the dispersions for the structure in Fig. 3a with varying widths. The results, shown in Fig. S6c, demonstrate that as N increases, the band gap shrinks, and the chiral anomaly bulk state persists, which is in agreement with the theoretical analysis. Moreover, we show the intensity and phase of the eigenstates at the K' valley, revealing vortex molecules uniformly distributed throughout the superlattice. Hence, the vortex (and the skyrmion) molecule bulk states are independent of the lattice width and are scalable.

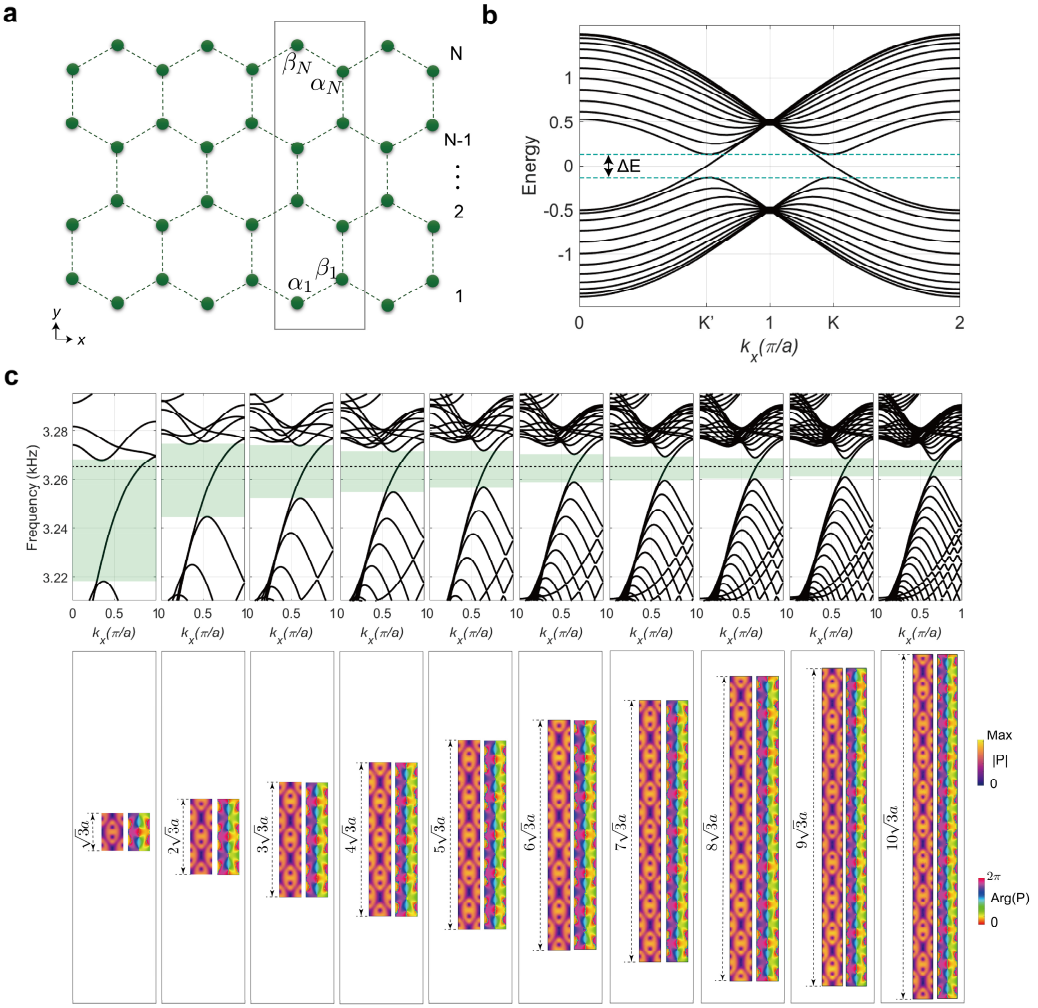

Fig. S6. **a**, Schematic of a graphene ribbon with N unit cells in the y-direction. **b**, Band structures of the graphene ribbon for $N = 12$. The green dashed lines highlight the energy window of the chiral anomaly bulk state. **c**, Top: Dispersion relations for the structure shown in Fig. 3a, but with varying width N. Bottom: Intensity and phase distributions of the eigenstates at K' valley for different N.

5. Manipulation of boundary potential

Figure S7a shows the finete p-orbitals graphene ribbon with a zigzag boundary along the y-direction. The Hamiltonian for this system is expressed as

$$H_{\text{ribbon}}(k_x, U_x, U_y) = t_L \begin{bmatrix} \mathcal{E}_1 & \mathcal{J} & 0 & 0 & 0 \\ \mathcal{J}^\dagger & \mathcal{B} & \ddots & 0 & 0 \\ 0 & \mathcal{J}^\dagger & \ddots & \mathcal{J} & 0 \\ 0 & 0 & \ddots & \mathcal{B} & \mathcal{J} \\ 0 & 0 & 0 & \mathcal{J}^\dagger & \mathcal{E}_2 \end{bmatrix}, \tag{S5.1}$$

under the basis $|\psi_{\text{ribbon}}\rangle = \left(\phi_{\alpha_1,p_x}, \phi_{\alpha_1,p_y}, \phi_{\beta_2,p_x}, \phi_{\beta_2,p_y}, \cdots, \phi_{\alpha_N,p_x}, \phi_{\alpha_N,p_y}, \phi_{\beta_N,p_x}, \phi_{\beta_N,p_y},\right)^T$. Here, $\mathcal{E}_{1,2}$, $\mathcal{B}$ and $\mathcal{J}$ represent the boundary, bulk, and link blocks, respectively, and are defined as

$$\mathcal{E}_1 = \begin{bmatrix} U_x & 0 & \frac{3}{2}\cos\frac{k_x}{2} & -\frac{\sqrt{3}}{2} i \sin\frac{k_x}{2} \\ 0 & U_y & -\frac{\sqrt{3}}{2} i \sin\frac{k_x}{2} & \frac{1}{2}\cos\frac{k_x}{2} \\ \frac{3}{2}\cos\frac{k_x}{2} & \frac{\sqrt{3}}{2} i \sin\frac{k_x}{2} & 0 & 0 \\ \frac{\sqrt{3}}{2} i \sin\frac{k_x}{2} & \frac{1}{2}\cos\frac{k_x}{2} & 0 & 0 \end{bmatrix}, \tag{S5.2}$$

$$\mathcal{E}_2 = \begin{bmatrix} 0 & 0 & \frac{3}{2}\cos\frac{k_x}{2} & -\frac{\sqrt{3}}{2} i \sin\frac{k_x}{2} \\ 0 & 0 & -\frac{\sqrt{3}}{2} i \sin\frac{k_x}{2} & \frac{1}{2}\cos\frac{k_x}{2} \\ \frac{3}{2}\cos\frac{k_x}{2} & \frac{\sqrt{3}}{2} i \sin\frac{k_x}{2} & U_x & 0 \\ \frac{\sqrt{3}}{2} i \sin\frac{k_x}{2} & \frac{1}{2}\cos\frac{k_x}{2} & 0 & U_y \end{bmatrix}, \tag{S5.3}$$

$$\mathcal{B} = \begin{bmatrix} 0 & 0 & \frac{3}{2}\cos\frac{k_x}{2} & -\frac{\sqrt{3}}{2} i \sin\frac{k_x}{2} \\ 0 & 0 & -\frac{\sqrt{3}}{2} i \sin\frac{k_x}{2} & \frac{1}{2}\cos\frac{k_x}{2} \\ \frac{3}{2}\cos\frac{k_x}{2} & \frac{\sqrt{3}}{2} i \sin\frac{k_x}{2} & 0 & 0 \\ \frac{\sqrt{3}}{2} i \sin\frac{k_x}{2} & \frac{1}{2}\cos\frac{k_x}{2} & 0 & 0 \end{bmatrix}, \tag{S5.4}$$

$$\mathcal{J} = \begin{bmatrix} 0 & 0 & 0 & 0 \\ 0 & 0 & 0 & 0 \\ 0 & 0 & 0 & 0 \\ 0 & 1 & 0 & 0 \end{bmatrix}, \tag{S5.5}$$

The boundary potential is controlled by the energy U_x and U_y at sites α_1, β_{N} for the p-orbitals $|p_x\rangle$ and $|p_y\rangle$. Based on the the characteristics of the vortex molecule eigenstates $|\psi\rangle$ at valleys

[Eq. (S1.10)], the uniform even and odd vortex molecule bulk states at the K' valley for the graphene ribbon can be written as

$$|\psi_{\text{ribbon,even},K'}\rangle = \mathcal{A}(1, i, 1, -i, \cdots, 1, i, 1, -i,)^T,$$
$$|\psi_{\text{ribbon,odd},K'}\rangle = \mathcal{A}(1, i, -1, i, \cdots, 1, i, -1, i,)^T. \quad \text{(S5.6)}$$

where $\mathcal{A}$ is the normalized constant. Thus, this constitutes a general inverse problem that can be solved numerically for the boundary conditions to select only one mode. Solving

$$H_{\text{ribbon}}(k_x, U_x, U_y)|\psi_{\text{ribbon},K'}\rangle = E_{\text{ribbon}}|\psi_{\text{ribbon},K'}\rangle, \quad \text{(S5.7)}$$

the boundary potentials are obtained as follows

$$\begin{cases} U_x = 0, U_y = -1 & \text{for even mode} \\ U_x = 0, U_y = +1 & \text{for odd mode} \end{cases}, \quad \text{(S5.8)}$$

Substituting the boundary conditions into H_{ribbon} and solving the eigenvalue equation yields the band structure shown in Fig. S7b. For the boundary conditions $(U_x = 0, U_y = -1)$ and $(U_x = 0, U_y = +1)$, the bands exhibit only even and odd mode dispersions within the bandgap, respectively. Furthermore, the chiralities at all sites are calculated according to[3]

$$\mathcal{C}_{i,j} \propto \text{Im}\left(\boldsymbol{\phi}_{i_j}{}^* \times \boldsymbol{\phi}_{i_j}\right), \quad \text{(S5.9)}$$

with $\boldsymbol{\phi}_{i_j} = \left[\phi_{i_j,p_x}, \phi_{i_j,p_y}\right]^T$, and $i = \alpha, \beta$; $j = 1,2, \cdots, \text{N}$. For the K' valley-locked even bulk states, the chirality is $+1$ (Ψ_+) at sites α and -1 (Ψ_-) at sites β, with a uniform distribution across all sites, as shown in the first plane of Fig. S7b. Conversely, for the K valley-locked odd bulk states, the chirality is reversed but remains uniformly distributed throughout the lattice. These results are consistent with the analysis in Supplementary Information 1. Moreover, as the boundary potential shifts from $U_y = -1$ to $U_y = +1$, the chiral anomaly bulk states evolve from the even mode to flat dispersions of edge states (the middle plane), and then to the odd mode. Meanwhile, the chirality is not uniform and approaches the boundary before returning to the bulk. Thus, the boundary potential in the p-orbital graphene ribbon provides a way to dynamically manipulate the molecule bulk state to achieve its chirality disappearance and reversal.

In the experiment, the dynamic manipulation of boundary site energy is achieved by changing the resonant frequency of p-orbital-like dipole modes. This is realized by introducing moderate amounts of silicone oil into the boundary cavities and altering the cavity depths, as shown in Fig. S7c. Figure S7d illustrates the resonance spectrum of the cavity as a function of the reduction in cavity depth δh. As the cavity depth decreases, or equivalently, as δh increases, the resonant frequency of the degenerate *p*-orbitals (indicated by the dark gray dots) increases, thereby enabling the manipulation of on-site energy.

We future calculate the band structure when $\delta h = 1.2\ mm$, as shown in Fig. S7e. Compared to the structure without boundary tuning in Fig. 3b, the propagating forward eigenstates shift K' to K valley-locking. Fig. S7f shows the acoustic pressure field distribution and spin texture, exhibiting odd vortex and skyrmion molecules, which is consistent with the theoretical result in Fig. S7b.

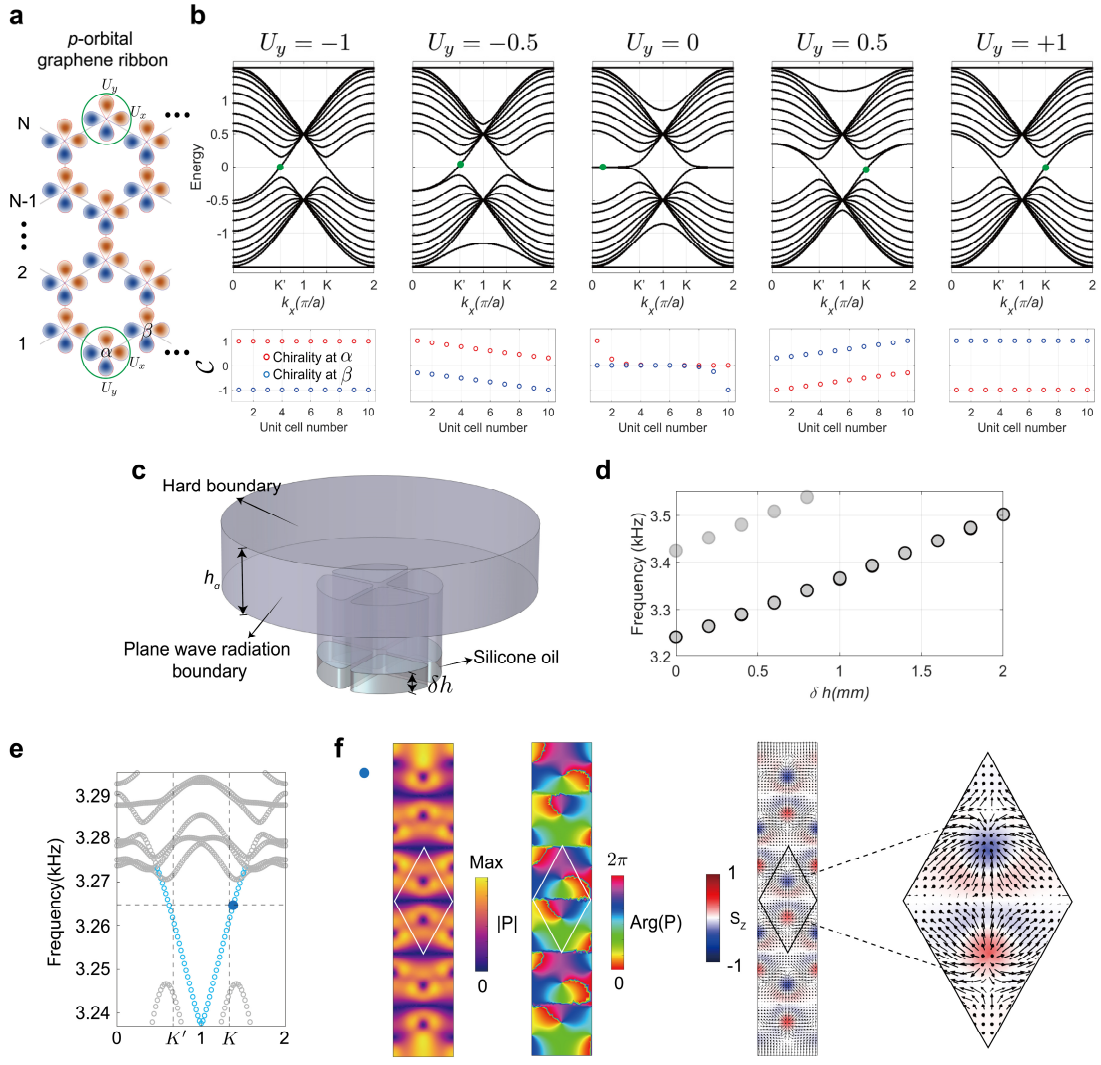

Fig. S7. **a**, Schematic of the p-orbitals graphene ribbon with N unit cells along the y-direction. **b**, Band structures of the graphene ribbon for $\mathrm{N} = 10$ with boundary potentials tuned to different values ranging from -1 to $+1$. The lower panels display the chirality distributions for the eigenstates highlighted by green dots. **c**, Schematic of a single-site cavity where silicone oil is introduced to alter the cavity depths. **d**, Resonance spectrum of the cavity in (c) as a function of the reduction in cavity depth δh. The degenerate p-orbitals $|p_x\rangle$ and $|p_y\rangle$ resonant modes are indicated by dark gray dots. **e**, Band structures for the lattice with the cavity depth change $\delta h = 1.2\ mm$. **f**, Acoustic pressure fields $|P|$, phase distributions $\mathrm{Arg}(P)$, and spin texture for the K valley-locked eigenstate (donated by the blue dot).

6. Displacement sensing based on spin skyrmion molecule

The spin component is not subject to diffraction, which makes the complex spin configurations of spin skyrmion molecules promising for sensing technologies. Our system exhibits a unique spin skyrmion molecule with inverse chirality located at sites α and β. Notably, this characteristic is protected by the inversion symmetry (see Supplementary Information 1). We introduce a steel globule to break this inversion symmetry, thus altering the spin density s_z distributions at the two sites. As shown in Fig. S8a, the globule moves along the $\pm y$ direction, perpendicular to the mirror plane of two sites. When the globule is positioned on the inversion center ($y = 0$), the local inversion symmetry between sites α and β remains intact. However, once the globule deviates from the inversion center, the inversion symmetry is broken, leading to a change in the spin density s_z for the skyrmion molecule. This change is detected by two sensors at sites α and β, both located at the same height. The variation in spin density, $\delta \mathrm{s_z}$, is defined as

$$\delta \mathrm{s_z} = \frac{\mathrm{s}_{z\alpha} + \mathrm{s}_{z\beta}}{\mathrm{s}_{z\alpha} - \mathrm{s}_{z\beta}}, \tag{S6.1}$$

where $\mathrm{s}_{z\alpha}$ and $\mathrm{s}_{z\beta}$ are the s_z components measured by the sensors at sites α and β, respectively. When $\mathrm{M}_{K',\mathrm{even}}$ skyrmion molecule is excited at 3.265 kHz, we move the globule along the y line and record the value of $\delta \mathrm{s_z}$. To reduce systematic errors, measurement is repeated ten times at each globule position, and the averaged value of $\delta \mathrm{s_z}$ is shown in Fig. S8b. Two conclusions can be drawn from the results:

(1) Variation in spin density originates from the breaking of inversion symmetry and is related to the degree of symmetry breaking. When the globule is positioned at the inversion center ($y = 0$), $\delta \mathrm{s_z}$ is zero, indicating that inversion symmetry remains intact. Nonzero values of $\delta \mathrm{s_z}$ appear only when the globule is at $|y| > 0$, reflecting the breaking of inversion symmetry.

Moreover, as the globule moves farther away from the inversion cneter, $\delta \mathrm{s_z}$ increases. Notably, $\delta \mathrm{s_z}$ exhibits a linear dependence along the position of the globule, making this system suitable for displacement sensing. When the globule is closer to one site, it reduces the spin density there and increases it at the other site. Specifically, when the globule is near site α, the positive spin density at α decreases, while the magnitude of negative spin density at site β increases, yielding a negative $\delta \mathrm{s_z}$. Conversely, placing the globule near site β induces a positive $\delta \mathrm{s_z}$. Benefiting from this approach, the experimental results demonstrate a displacement resolution of $\lambda/209.4$ ($\lambda = 10.47$ cm is the excitation wavelength) for the globule.

(2) Displacement sensing is effective for subwavelength-size objects. Shrinking the diameter of the globule from $\lambda/6.98$ to $\lambda/7.22$ and subsequently to $\lambda/7.48$ decreases the degree of inversion symmetry breaking, leading to a reduction in $\delta \mathrm{s_z}$ at the same globule's positions. However, $\delta \mathrm{s_z}$ maintains its linear relationship with displacement, confirming that this spin-based displacement sensing method remains viable even for subwavelength-scale objects.

In conclusion, our experiment highlights the subwavelength features of spin skyrmion molecules, demonstrating their promising potential for sensing applications.

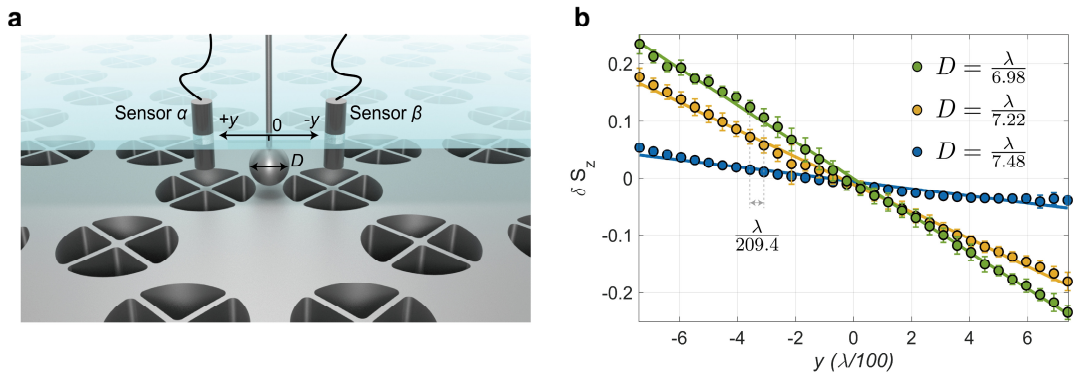

Fig. S8. **a**, Schematic of the displacement sensing experimental setup. A steel globule moves along the line connecting the two centers of skyrmion, while two sensors at sites α and β detect changes in the spin density. **b**, Variation of the spin density δs_z as a function of the globule's position y, measured using globules with different diameters. Each measurement is repeated ten times, and the averaged results are presented.

7. Sample design

Figure S9a shows the top view of an open resonant cavity with a radius r. A block plate with width w divides the circular cavity into four sections, and the small cavity's circular chamfer has a radius r_c. We calculated its resonance spectrum, depicted in Fig. S9b, where the degenerate p-orbital-like dipole resonances appear at 3.24 kHz. Notably, an acrylic ceiling serving as a hard boundary, depicted in Figs. S7c and 2c, is placed above the cavity to prevent radiation losses. The acoustic wave of two p-orbital modes exhibits an evanescent field, decaying along the out-of-plane (z-axis), as shown in Fig. S9c.

We then calculated the band structure for the acoustic lattice shown in Fig. 2c, considering various cavity depths h_c, as shown in Fig. S9d, which includes the acoustic line indicated by the red dash line. When $h_c = 2.2$ cm, although most of the p-orbital bands extend beyond the bound region (i.e., above the sound line), the Dirac points remain within the acoustic line. As h_c increases, or equivalently, as the cavity deepens, it shifts most of the p-orbital bands below the acoustic line but also narrows the bandwidth. Consequently, we selected a cavity depth of $h_c = 2.2$ cm to achieve a broader bandwidth for the p-orbital bands.

Furthermore, to prevent radiation losses for those portions of the p-orbital band lying above the acoustic line, we introduce an acrylic ceiling to form a propagating channel of height h_a, as shown in Fig. 2c. This channel is sufficiently narrow to preclude out-of-plane modes, thus confining the acoustic field to the surface of sample. Increasing h_a degrades the Bloch modes of the p-orbital located above the acoustic line, as illustrated in Fig. S9e. When h_a exceeds 3.6 cm, the dispersions of these p-orbital become significantly distorted. Hence, we chose $h_a = 1.6$ cm in our experimental setup.

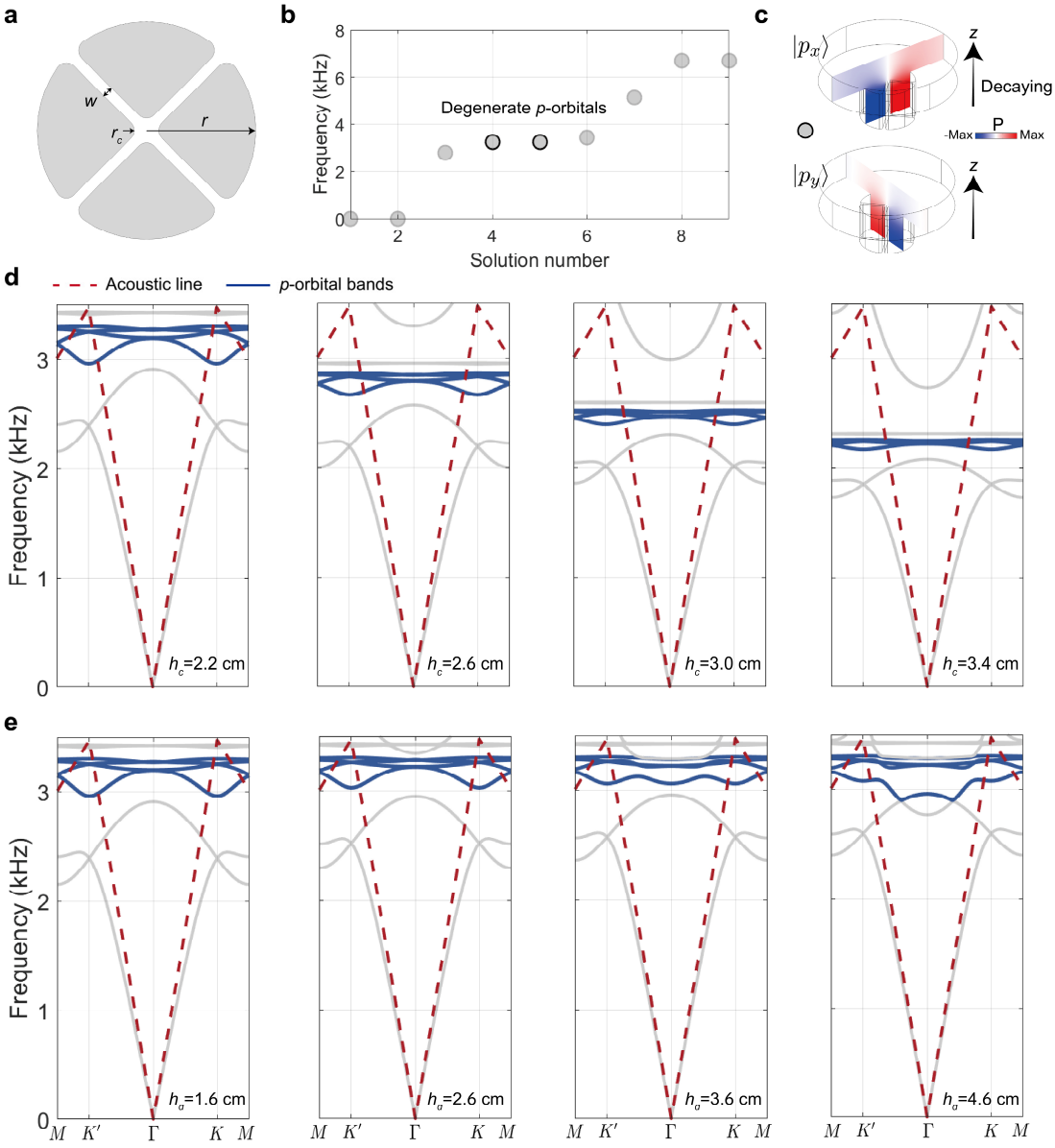

Fig. S9. **a**, Top view of an open resonant cavity. **b**, Resonance spectrum of a single sublattice cavity composed of four petaloid cavities in Fig. 2c. **c**, Acoustic pressure fields in the y-z and x-z cross-sections for the p-orbital resonant modes. **d**, Band structure of the acoustic lattice in Fig. 2c for different cavity depths h_c. The red dashed line marks the acoustic line, and the blue line denotes the p-orbital bands. **e**, Band structure for various channel heights h_a.

8. Three-dimensional acoustic particle velocity sensing technique

The homemade acoustic particle velocity and pressure sensor is used to separately detect the amplitude and phase of the v_x, v_y, v_z and P components of spoof surface acoustic waves. As shown in Fig. S10, this sensor comprises three groups of suspended wires above a silicon substrate, corresponding to the three velocity measurement directions, and a capacitive pressure MEMS sensor for acoustic pressure detection. These suspended wires are heated wires with temperature-dependent resistance. An incident acoustic wave induces a temperature difference between wires, causing a difference in resistance that is proportional to the local acoustic particle velocity. The sensor is oriented perpendicular to the sample surface such that two wire groups remain parallel to the surface, and the third group is perpendicular.

In the experiment, the sensor is moved point-by-point to measure the acoustic velocity and pressure fields. An additional audio input channel is connected to the same data acquisition module and serves as a reference signal. A Fast Fourier Transform (FFT) is performed on each acquired time-domain signal segment to obtain frequency-domain data

$$\begin{aligned}\tilde{\mathbf{v}}_{\text{signal}}(\mathbf{r},\omega) &= \mathcal{F}\left[\mathbf{v}_{\text{signal}}(\mathbf{r},t)\right],\\ \tilde{P}_{\text{signal}}(\mathbf{r},\omega) &= \mathcal{F}\left[P_{\text{signal}}(\mathbf{r},t)\right],\\ \tilde{E}_{\text{ref}}(\mathbf{r},\omega) &= \mathcal{F}[E_{\text{ref}}(\mathbf{r},t)],\end{aligned} \tag{S8.1}$$

The velocity and pressure are then obtained via

$$\begin{aligned}\tilde{\mathbf{v}}(\mathbf{r},\omega) &= \left|\tilde{\mathbf{v}}_{\text{signal}}(\mathbf{r},\omega)\right| e^{i\boldsymbol{\varphi}_v(\mathbf{r},\omega)},\\ \tilde{P}(\mathbf{r},\omega) &= \left|\tilde{P}_{\text{signal}}(\mathbf{r},\omega)\right| e^{i\varphi_p(\mathbf{r},\omega)},\end{aligned} \tag{S8.2}$$

where

$$\begin{aligned}\boldsymbol{\varphi}_v(\mathbf{r},\omega) &= \boldsymbol{\varphi}\left[\tilde{\mathbf{v}}_{\text{signal}}(\mathbf{r},\omega)\right] - \varphi[\tilde{E}_{\text{ref}}(\mathbf{r},\omega)],\\ \varphi_p(\mathbf{r},\omega) &= \varphi\left[\tilde{P}_{\text{signal}}(\mathbf{r},\omega)\right] - \varphi[\tilde{E}_{\text{ref}}(\mathbf{r},\omega)],\end{aligned} \tag{S8.3}$$

We can further add the time dynamic term $e^{i\omega t}$ as

$$\begin{aligned}\tilde{\mathbf{v}} &= \tilde{\mathbf{v}}(\mathbf{r},\omega)e^{i\omega t},\\ \tilde{P} &= \tilde{P}(\mathbf{r},\omega)e^{i\omega t},\end{aligned} \tag{S8.4}$$

Figure S11a shows raw measured results of the amplitudes $\left|\tilde{\mathbf{v}}_{\text{signal}}(\mathbf{r},\omega)\right|$ and $\left|\tilde{P}_{\text{signal}}(\mathbf{r},\omega)\right|$ in the boxed region of Fig. S3a. Due to inevitable systematic losses, particularly since the 2D propagation space between the acrylic ceiling and the steel plate is not fully enclosed, the amplitude decreases with propagation distance. Because the vortex and skyrmion molecule states exhibit uniformity along the width direction of the waveguide, the loss can be captured by

$$\begin{aligned}\mathbf{I}_{\text{v}}(x,\omega) &= \int_0^{max(y)} \left|\tilde{\mathbf{v}}_{\text{signal}}(\mathbf{r},\omega)\right| dy,\\ I_P(x,\omega) &= \int_0^{max(y)} \left|\tilde{P}_{\text{signal}}(\mathbf{r},\omega)\right| dy.\end{aligned} \tag{S8.5}$$

Figure S11b shows $I_P(x,\omega)$ and $\mathbf{I}_{\text{v}}(x,\omega)$, both decreasing as increases x, indicating amplitude reduction over distance. Notably, this amplitude loss does not affect the phase-dependent features of vortex and spin. To more clearly visualize the modal fields, we normalize the velocity and pressure amplitudes as

$$\begin{aligned}\tilde{\mathbf{v}}_{\text{nor}} &= \tilde{\mathbf{v}}/\mathcal{P}[\mathbf{I}_{\text{v}}(x,\omega)],\\ \tilde{P}_{\text{nor}} &= \tilde{P}/\mathcal{P}[I_P(x,\omega)],\end{aligned} \tag{S8.6}$$

where $\mathcal{P}$ denotes a least squares cubic polynomial fit. The fitting curves of $\mathbf{I}_{\text{v}}(x,\omega)$ and $I_P(x,\omega)$ are indicated by black lines in Fig. S11b. The spin fields (derived from the normalized velocity

fields) and the normalized pressure fields and are shown in Figs. 3c and 3d. By varying the time factor $e^{i\omega t}$, we also show the wave dynamics in the acoustic pressure and velocity fields through Movies S1 and S2. Subsequent measurements in Figs. 4c and 4d and Movies S3 and S4 are carried out using the same experimental setup and data processing methods.

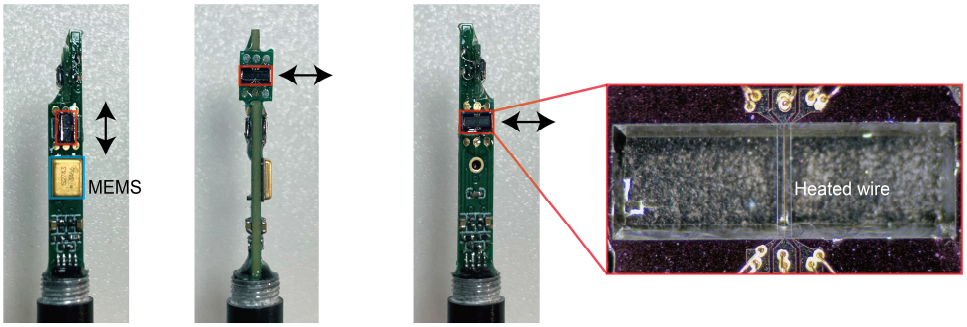

Fig. S10. Photos illustrating three different faces of our acoustic particle velocity and pressure sensor, featuring three groups of suspended wires for velocity measurements and a MEMS-based pressure sensor.

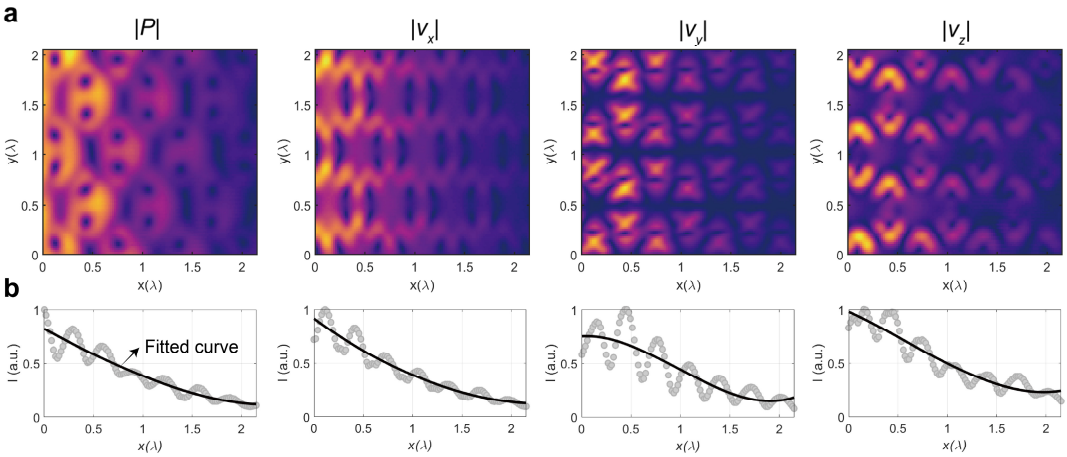

Fig. S11. **a**, Raw measurements of the amplitudes $\left|\tilde{\mathbf{v}}_{\text{signal}}(\mathbf{r},\omega)\right|$ and $\left|\tilde{P}_{\text{signal}}(\mathbf{r},\omega)\right|$. **b**, The integral of the y section for $\left|\tilde{\mathbf{v}}_{\text{signal}}(\mathbf{r},\omega)\right|$ and $\left|\tilde{P}_{\text{signal}}(\mathbf{r},\omega)\right|$ as functions of the propagation distance x. The dots represent experimental data, and the black lines show the results of a least squares cubic polynomial fit.

9. Molecule decomposition based on simulation results

We extract simulation data from the eigenstates at the K and K' valley in the band structure calculations to perform molecule decomposition, paralleling the analysis in Fig. 5. The results shown in Fig. S12 reveal skyrmions with skyrmion numbers of ± 1, which, aside from experimental errors, are consistent with the measurements in Fig. 5. These findings further confirm the topological quantization of skyrmions, highlighting their quasiparticle nature and demonstrating the effectiveness of using molecules to stabilize, transport and manipulate skyrmions.

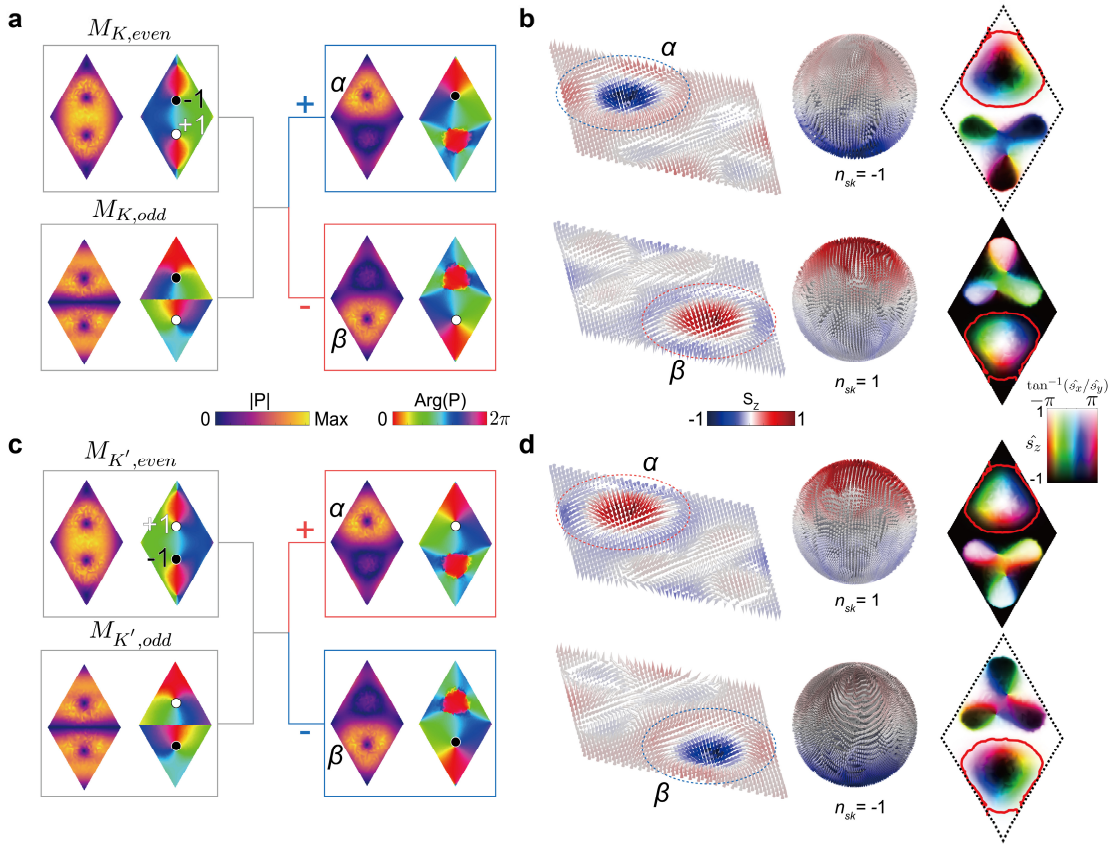

Fig. S12. **a-b**, Superposition of the even and odd molecules at the K valley based on simulation data. **a**, Scalar pressure field superposition. **b**, Spin vector field superposition. The results demonstrate the decoupling of the vortex/skyrmion pairs, with their individual topological properties isolated at different sublattices. This is corroborated by the quantized skyrmion numbers n_{sk}, the stereographic projections of the spin vector field (within the dashed circular regions) and the distribution of the reconstructed three-component spin vector field (encoded by the brightness and colors). **c-d**, The same as **a-b**, but for the K'-valley decomposition.

References

1. Xu S. , Wu C. Orbital-active Dirac materials from the symmetry principle. *Quantum Front*. **1**, 24 (2022).
2. Lu, J. *et al*. Observation of topological valley transportof sound in sonic crystals. *Nat. Phys.* **13**, 369–374 (2017).
3. Varshalovich, D. A., Moskalev, A. N. & Khersonskii, V. K. *Quantum Theory of Angular Momentum* (World Scientific, United States, 1987).